A

Theory appendices

A.1 Electrostatic Discharge and Paschen's law

This section is a explanation of the electrostatic discharge (ESD) phenomenon that can occur between two conductors separated by a gas or a plasma. The idea of this section is not to derive the Paschen's law expression but to understand the physic hidden behind the associated curve.

First, an ESD occurs when an electric field generates a conductive ionised path between two conductors, an anode and a cathode. At the moment when the path is generated, the electrons can flow through it like in a conductor. The Paschen's curve is represented in figure A.1. This curve represents the breakdown voltage V_{BD} of a gas with respect to the product of the gas pressure p and the distance between electrodes d. When the voltage between the electrodes is beyond the breakdown voltage, an ESD occurs. The curve is characterized by a minimum value V_{min}.

In order to understand the curve, let's represents an experimentation with two electrodes separated by a distance d and with a fixed voltage difference V (Figure A.2a). The resulting electric field between the electrodes is $E = \frac{V}{d}$. The gas located between the electrodes has a homogeneous pressure p that is varied. The mean free path of an electron λ is the average distance between its collision with neutral atoms in the gas. Logically, the mean free path is inversely proportional to the pressure : $\lambda \propto p^{-1}$. For a high pressure, there are more atoms and then the collisions are more frequent. Let's consider a free electron in the cathode (red ball). This one is accelerated by the electric field, then it collides with a neutral atom (red ball + white ball) . If the electron has enough energy before the collision, it can ionise the atom which results in an electron and a positive ion (white ball). The two electrons, the first one and the other generated by ionisation, are both accelerated with the electric field. An avalanche phenomenon is then generated : the electrons ionise the atoms and are then multiplied. The ions are left and form a conductive path. The condition for an ionisation is that the electrons need to have more energy than the ionisation energy of the atom before the collision :

$$W_e > W_{ionisation} \tag{A.1}$$

where $W_{ionisation}$ depends on the atom nature and the electron energy is given with the kinetic energy :

$$W_e = \frac{1}{2} m_e v^2 = E q_e \lambda \tag{A.2}$$

where m_e is the electron mass and q_e is the electron charge. Therefore, the electron energy before collision depends on the electric field applied E. There are two regions on the Paschen's curve :

- In the right side of V_{min}, the pressure is high and the mean free path (λ) is low. The electron accelerated by the electric field does not have time to reach a sufficient speed before a collision. Therefore, the electron energy is lower than the ionisation energy and no ionisation happens. Then, no avalanche is ignited and no positive ion path is generated.

- In the left side of V_{min}, the pressure is low and the mean free path (λ) is high. Therefore, the electron will collide the anode before having a chance to ionise an atom. Once again, no avalanche effect can be ignited.

The experiment can be made for a fixed pressure and a varying distance. If d is low compared to the mean free path of electrons, no avalanche is created. If d is too high, the electric field is lower, the electrons are not enough accelerated and they cannot ionise the atoms during a collision.

The problem is that for a given pressure, it is really complicated to control the distance between the electrodes. For example, let's consider two perpendicular conductors (Figure A.2b). There is not only one distance between the conductors, but there is a range of distances (d_1,d_2,d_3,...). Therefore, if the voltage between the electrodes is higher than the minimal voltage ($V > V_{min}$), the electrons would find the perfect distance by itself and an ESD would occur. That is why, the voltage of the slip rings cannot exceed 110V for space applications.

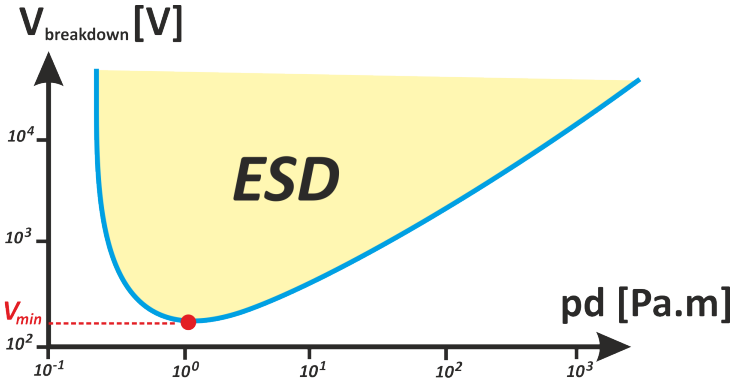

Figure A.1 – Paschen curve : function of breakdown voltage with respect to the pressure and distance product

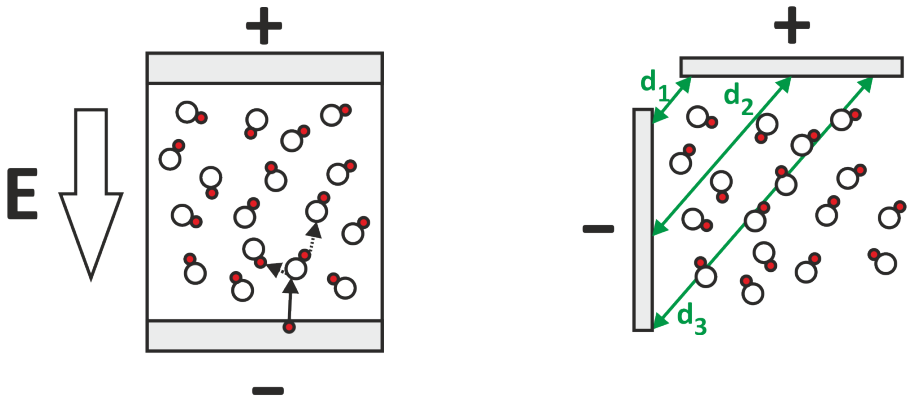

(a) Experiment with two parallel electrodes (d constant)

(b) Experiment with two perpendicular electrodes (p constant)

Figure A.2

A.2 Zero Voltage Switching

This part is an introduction to the Zero Voltage Switching in a Dual Active Bridge.

In a Switch-Mode Power Supply (SMPS), there are two kinds of losses happening in the transistors: conducting and switching losses. The conducting losses are produced because of the current passing through the transistor *on*-state resistance ($R_{ds,on}$). The second losses are switching losses. Those losses happen while a switch turns on or turns off. In reality, a transistor has a parasitic capacitance between the drain and the source (C_{ds}). This capacitance can be seen on the half-bridge switches of figure A.3. This capacitance implies that the voltage across the transistor cannot change instantaneously. Therefore, during a switching, both voltage and current are applied on the switch and a large amount of energy is lost. However, it is possible to cancel those losses by the use of a *Zero Voltage Switching* (ZVS) control.

The ZVS principle is represented in figure A.3. First, a reversed diode needs to be connected in parallel of each transistor. The different steps of the switching transition for a ZVS control are given for the case of a switch from S_1 to S_2 :

- $\underline{t < 0}$: initially, S_1 is *on* and the current (I_L) is flowing through it. The output voltage is $V_o = V_{dc}$. Therefore, $C_{ds,2}$ is charged but $C_{ds,1}$ is not ($Q_1 = 0$ and $Q_2 = C_{ds}V_{dc}$).
- $\underline{0 < t < t_{dead}}$: at the time when S_1 is turned-off, the charge of each capacitance are the same as before and the output voltage is the same also. Therefore, the current is flowing through $C_{ds,1}$ and $C_{ds,2}$ in order to respectively increase and decrease the charge. The output voltage is then decreased until it reaches the threshold voltage of the diode (V_{th}). When this voltage is reached, no more current is flowing through $C_{ds,1}$ and $C_{ds,2}$ and this is the diode that conducts the current. At that moment, the voltage around the switch is low ($V = V_{th}$) and S_2 can finally be turned-on.
- $\underline{t_{dead} < t}$: S_2 is *on* and conducts all the current. No more current is flowing through the diode.

As explained, the voltage drop across each switch is equal to zero when current is flowing. The time during which both switches are *off* is called the *dead time* (t_{dead}). This time depends on the inductor current (I_L) and the capacitances charge (Q):

$$t_{dead} = \frac{\Delta Q_1 - \Delta Q_2}{I_L} = 2 * \frac{C_{ds}V_{dc}}{I_{L,max}} \tag{A.3}$$

At low load, the current I_L risks to be not enough to ensure a ZVS mode. However, the magnetizing current I_μ can compensate if the magnetizing inductance is not too large.

The principle can be applied for the inverse case ($S_2 \rightarrow S_1$). If the ZVS mode is respected, the losses generated by the DAB can be estimated by the conductive losses of the transistors :

$$P_{dab} = 4 * R_{ds,on} * I_{L,rms}^2 \tag{A.4}$$

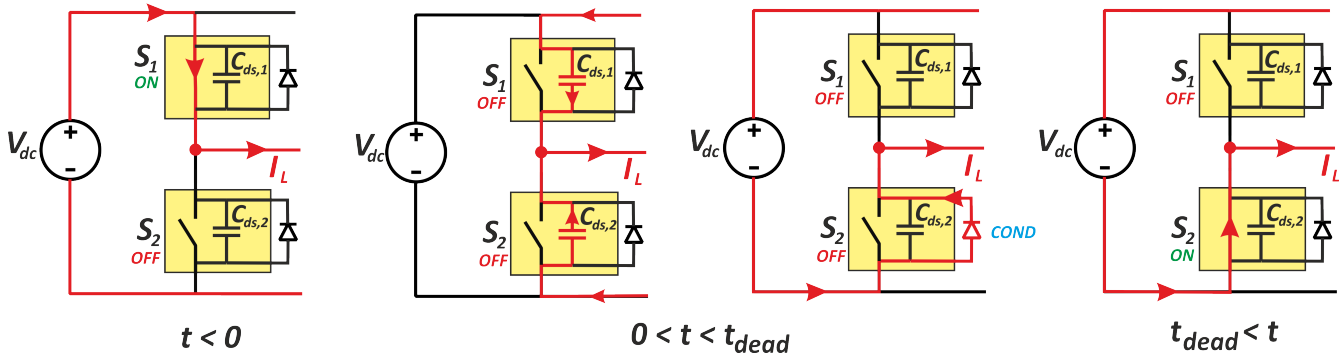

Figure A.3 – Zero Voltage Switching : Principle

A.3 Voltage, current and flux density waveforms in the transformer

This section is a clarification of the different voltage, current and flux density waveforms involved in the transformer and inductor used in a Dual Active Bridge (DAB). The explanation of the DAB operation is available in section 1.4.4. Figure A.4 presents the different waveforms involved in the transformer inductive model.

First, the equation linking the voltage and the current of an inductance is :

$$i_L(t) = \frac{1}{L}\int v_L(t)dt \tag{A.5}$$

Afterwards, the inductance definition can provide a link between the flux density in an inductor and the current flowing in it :

$$L = \frac{\phi}{i} \rightarrow B_L(t) \propto i_L(t) \tag{A.6}$$

The voltage applied on the magnetizing inductance corresponds to a simple square waveform generated by the primary side full-bridge of the DAB. The integration of a square waveform is a triangular waveform. Therefore, the flux density in the transformer has a trapezoidal waveform.

The voltage applied on the series inductance corresponds to the difference between two square waveform delayed with a phase-shift ($D = \frac{\phi}{\pi}$). This phase-shift is the control variable of the DAB. The integration of such a waveform gives a trapezoidal waveform with a duty cycle $D = \frac{t_{ramp}}{T}$. Therefore, the current flowing through the series elements of the transformer and the inductor (winding resistances and inductances) are trapezoidal. Moreover, the flux density in the external inductor core is also trapezoidal.

The harmonic content of trapezoidal and triangular waveforms are described in next section.

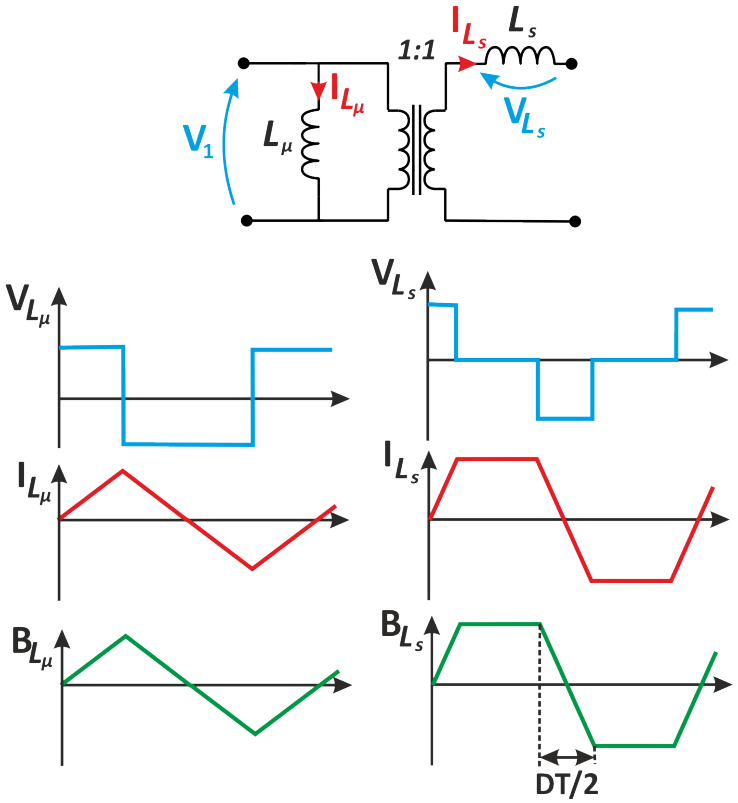

Figure A.4 – Transformer waveforms : representation of voltage, current and flux density

A.4 Trapezoidal waveform : harmonic content

In this section, the harmonic content of a trapezoidal waveform is analysed. A comparison is done between the triangular, the trapezoidal and the square waveforms.

First, a zero offset signal with a trapezoidal waveform $s_{trap}(t)$ can be expressed with the Fourier series (Figure A.5) :

$$s_{trap}(t) = S_{max} * \sum_{n=1,3,...}^{\infty} \left[\frac{16}{\pi^2 n^2} \cdot \frac{sin(n\phi/2)}{(2\phi\pi)^2} \right] \cdot sin\left(2\pi \cdot n \cdot ft\right) \tag{A.7}$$

where $\phi = \pi D$ is the phase-shift angle corresponding to the duty-cycle ($D = \frac{t_{ramp}}{T}$) and n is the number of the n^{th} harmonic. As it can be seen, only the odd harmonics are considered.

The triangular waveform corresponds to the trapezoidal waveform with a duty-cycle $D = 1$ ($\phi = 180$). The triangular waveform signal is expressed as :

$$s_{tri}(t) = S_{max} * \sum_{n=1,3,...}^{\infty} \left[\frac{16}{\pi^2 n^2} \right] \cdot sin\left(2\pi \cdot n \cdot ft\right) \tag{A.8}$$

The square waveform corresponds to the trapezoidal waveform with a duty-cycle $D = 0$ ($\phi = 0$). The square waveform signal is expressed as :

$$s_{square}(t) = S_{max} * \sum_{n=1,3,...}^{\infty} \left[\frac{4}{\pi n} \right] \cdot sin\left(2\pi \cdot n \cdot ft\right) \tag{A.9}$$

The expression inside the brackets of each equation correspond to the norm of the harmonics. It can be seen that for a square waveform, the harmonic norm is inversely proportional to its number (n) while, for a triangular waveform, the harmonic norm is inversely proportional to its number squared. Therefore, the harmonic content for a triangular waveform is lower than for a square waveform. The harmonic content increases with a decreasing duty-cycle ($D \to 0$). Therefore, it is important to not use a too small duty-cycle for the Dual Active Bridge because the harmonics generates an increase of losses (see sections 2.2 and 2.3).

The Root Mean Square (RMS) value of a trapezoidal waveform is :

$$s_{trap,rms} = S_{max} * \sqrt{1 - \frac{2D}{3}} \tag{A.10}$$

The rms values of square and triangular waveforms can be derived from the last equation :

$$\begin{aligned} s_{tri,rms} &= \frac{S_{max}}{\sqrt{3}} \\ s_{square,rms} &= S_{max} \end{aligned} \tag{A.11}$$

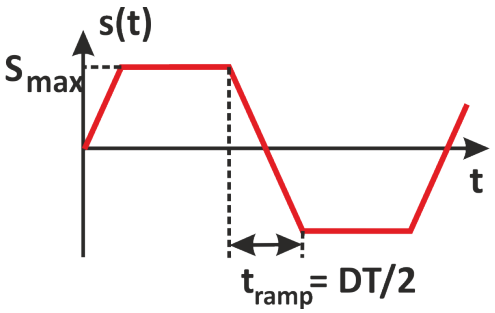

Figure A.5 – Trapezoidal waveform

A.5 Reluctance formulae derivation

The *Hopkinson's law* introduces the concept of reluctance ($\mathcal{R}$) which can be described as the ability of a material to oppose to a magnetic field :

$$\mathcal{R} = \frac{\mathcal{F}}{\phi} = \frac{\int \mathbf{H} \cdot d\mathbf{l}}{\int \mathbf{B} \cdot d\mathbf{A}} \tag{A.12}$$

Likewise the resistance, the reluctance only depends on geometry and material properties.

In this section, the equation of the reluctances are derived. The equation is not the same for all reluctances. Indeed, the formula depends on the magnetic flux direction in the reluctance shape. It also depends on the magnetic flux distribution within the reluctance cross section (homogeneous or linear). In this section, three cases of reluctance are derived : with a homogeneous axial flux, with a homogeneous radial flux and with a linear axial flux. Figure A.6 presents the flux orientation for each case.

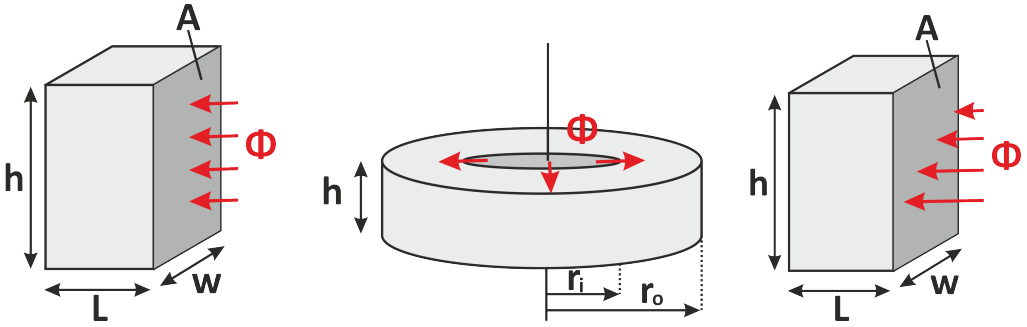

(a) Axial constant flux (b) Radial constant flux (c) Axial linear flux

Figure A.6 – Representation of the reluctance dimensions for formula

Reluctance for homogeneous axial flux

This is the simplest case of a reluctance. As the flux density (B) is constant over the entire area (A) and along the entire path (L), the reluctance equation is :

$$\mathcal{R}_{cst,axial} = \frac{\int \mathbf{H} \cdot d\mathbf{l}}{\int \mathbf{B} \cdot d\mathbf{A}} = \frac{H \cdot L}{B \cdot A} = \frac{L}{\mu \cdot A} \tag{A.13}$$

Reluctance for homogeneous radial flux

For this case, the flux conservation in the radial direction implies that the magnetic flux density has the following shape :

$$B = B(r) = \frac{C}{r} \tag{A.14}$$

where C is a constant. By injecting the previous equation in the reluctance definition, the reluctance for a radial flux is expressed as :

$$\mathcal{R}_{cst,radial} = \frac{\int \mathbf{H} \cdot d\mathbf{l}}{\int \mathbf{B} \cdot d\mathbf{A}} = \frac{\int_{r_i}^{r_o} \mu^{-1} \frac{C}{r} \cdot dr}{\int_0^{2\pi} \frac{C}{r} \cdot r d\theta h} = \frac{ln(r_o/r_i)}{\mu \cdot 2\pi \cdot h} \tag{A.15}$$

Reluctance for linear axial flux

For a linear axial flux, the reluctance is calculated by considering the change of H with the y-position :

$$H(x) = \frac{n(y)i}{L} = \frac{Ni \cdot y}{L \cdot h} \tag{A.16}$$

Moreover, the surface area sees more flux with the y-position. Equation A.12 can be expressed as :

$$\begin{aligned} \mathcal{R}_{lin,axial} &= \frac{\mathcal{F}}{\phi} \\ &= \frac{Ni}{\int \mu \frac{Ni \cdot \frac{y}{h}}{L \cdot h} \frac{y}{h} w dy} \\ &= \frac{L \cdot w^2}{\mu h \int_0^w y^2 dx} \\ &= 3 * \frac{L}{\mu \cdot h \cdot w} \\ &= 3 * \mathcal{R}_{cst,axial} \end{aligned} \tag{A.17}$$

A.6 Iron losses : improved Generalized Steinmetz Equation for trapezoidal waveforms

The volumetric power losses generated by a zero-offset sinusoidal flux density can be evaluated by the original *Steinmetz equation* :

$$P_{v,sin} = k \cdot f^{\alpha} \cdot \hat{B}^{\beta} \tag{A.18}$$

where k, α and β are properties of the magnetic material and are determined by experimentation. $\hat{B}$ is the flux density peak value.

However, flux density in the Dual Active Bridge converter are zero-offset trapezoidal or triangular waveforms. In literature, an adaptation of the *Steinmetz equation* for non-sinusoidal waveforms was made [23]. It is called the *improved Generalized Steinmetz Equation (iGSE)* and is expressed as follows :

$$P_{v,trap} = \frac{1}{T}\int_0^T k_i \left|\frac{dB}{dt}\right|^{\alpha} (\Delta B)^{\beta-\alpha} dt \tag{A.19}$$

where ΔB is peak-to-peak flux density and

$$k_i = \frac{k}{(2\pi)^{\alpha-1}\int_0^{2\pi} |cos\theta|^{\alpha} 2^{\beta-\alpha} d\theta} \tag{A.20}$$

For a trapezoidal waveform, the integration can be divided in two parts corresponding to the trapezoid plateaux and the trapezoid ramps. During a plateau, the flux density is constant. So, its derivative with respect to time is null and no losses are generated. Another point is that the same amount of losses are generated during increasing and decreasing transition. Therefore, equation (A.19) can be written as :

$$\begin{aligned} P_{v,trap} &= \frac{1}{T} \cdot k_i \left(\frac{\Delta B}{DT/2}\right)^{\alpha} (\Delta B)^{\beta-\alpha} DT && \text{(A.21)} \\ &= k_i \cdot 2^{\alpha} \left(\frac{1}{T}\right)^{\alpha} (\Delta B)^{\beta} D^{1-\alpha} && \text{(A.22)} \\ &= k_i \cdot 2^{\alpha+\beta} f^{\alpha} (\hat{B})^{\beta} D^{1-\alpha} && \text{(A.23)} \\ &= \frac{k \cdot f^{\alpha} \cdot \hat{B}^{\beta} \cdot D^{1-\alpha} \cdot 2^{2\alpha}}{(2\pi)^{\alpha-1} 4 \int_0^{\pi/2} (cos\theta)^{\alpha} d\theta} && \text{(A.24)} \end{aligned}$$

The integration term can be expressed with the *Gamma function* (Γ) as :

$$\int_0^{\pi/2} (cos\theta)^{\alpha} d\theta = \frac{\sqrt{\pi}}{2} \frac{\Gamma\left(\frac{\alpha+1}{2}\right)}{\Gamma\left(\frac{\alpha}{2}+1\right)} \tag{A.25}$$

Finally the final equation found for the volumetric power losses generated by a trapezoidal waveform is :

$$P_{v,trap} = k \cdot f^{\alpha} \cdot \hat{B}^{\beta} \cdot D^{1-\alpha} \cdot 2^{\alpha} \cdot \pi^{0.5-\alpha} \cdot \frac{\Gamma\left(\frac{\alpha}{2}+1\right)}{\Gamma\left(\frac{\alpha+1}{2}\right)} \tag{A.26}$$

This expression is composed of three terms. The first one corresponds to the original *Steinmetz equation* (A.18) with an equivalent sinusoidal waveform. The second part is related to the trapezoid duty-cycle (D). It can be seen that for a same period, the losses increase with the trapezoid stiffness. The last term is a constant depending on the α coefficient of the magnetic material. A typical value for this coefficient for ferrite materials is $\alpha = 1.5$. For this value the power losses expression can be replaced as :

$$P_{v,trap}(\alpha = 1.5) = 0.915 \cdot k \cdot f^{1.5} \cdot \hat{B}^{\beta} \cdot D^{-0.5} \tag{A.27}$$

For a triangular waveform, the expression is:

$$P_{v,tri}(\alpha = 1.5) = 0.915 \cdot k \cdot f^{1.5} \cdot \hat{B}^{\beta} \tag{A.28}$$

The core losses generated for a triangular waveform are 8.5% lower than for a sinusoidal waveform with same frequency and peak value. This is the case of the transformer core losses.

In the external inductor, the flux density is a trapezoidal waveform with a duty-cycle $D = 0.25$. The expression of the associated core losses is :

$$P_{v,tri}(\alpha = 1.5, D = 0.25) = 1.83 \cdot k \cdot f^{1.5} \cdot \hat{B}^{\beta} \tag{A.29}$$

The core losses generated for a trapezoidal signal with $D = 0.25$ are 83% higher than for a sinusoidal waveform with same frequency and peak value.

The conclusion is that the core losses increase with a decreasing trapezoid duty-cycle D.

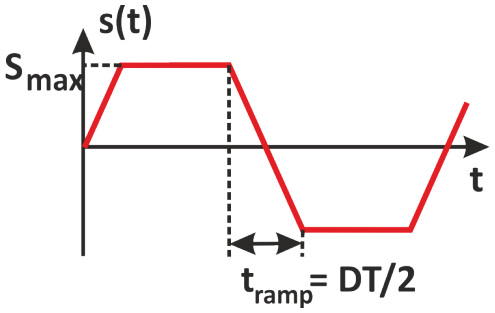

Figure A.7 – Trapezoidal waveform

A.7 Proximity effect

The *Proximity effect* is a phenomenon happening in multi-layers and multi-strands windings and which is often neglected. However, that has an important impact on the equivalent AC resistance R_{ac}. This is why this effect is deeply analysed in this section [20].

By *Ampere's law*, a high-frequency current $i(t)$ flowing through a strand produces a high-frequency magnetic flux. Inside of this strand, the flux produces eddy-currents and the net current is pushed on the wire surface. In a same way, this flux produces eddy-currents in the other strands which are located next to this one. Those eddy-currents interfere with the initial currents flowing in the strands and the AC resistance is increased. In order to understand this effect, the case of large wires ($d \gg \delta$) is first analysed. Afterwards, the general case is inquired.

Case 1 : $d \gg \delta$

A first way to see the effect is to take two parallel wires with a diameter highly larger than the *skin depth* ($d \gg \delta$). The first one (w_1) is excited with a high-frequency current $i_1(t)$ and the other (w_2) is open-circuited ($i_2(t) = 0$). A FEM and schematic representation of the proximity effect for this case are depicted in figure A.8. As it can be seen, w_1 produces a magnetic flux (ϕ) that generates eddy-currents opposed to i_1 in the left side of the wire. As w_2 is open-circuited, no net current is flowing through it and eddy-currents are generated on the right side of w_2 such as $i_{2,l} = -i_{2,r}$. If $d \gg \delta$ and the two wires are very close, the current $i_{2,l}$ is equal and opposite to $i_1(t)$.

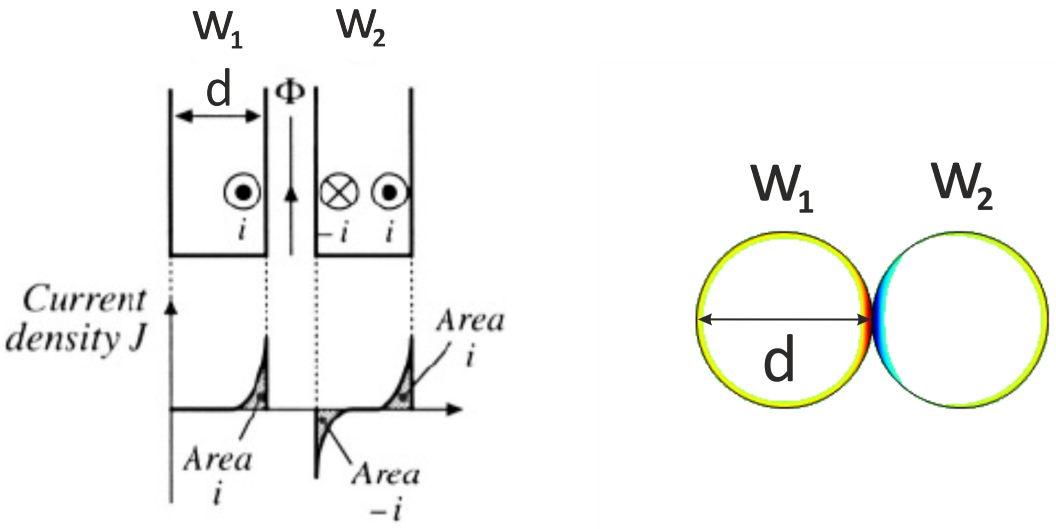

(a) Schematic representation [20]

(b) Finite Element Method representation (Comsol)

Figure A.8 – Proximity effect in two wires : w_1 is excited with $i(t)$ and w_2 is open-circuited.

Now, let's consider the case of a multi-layer transformer. Figure A.9 represents a symmetric concentric transformer cross section. At low frequency, the same current is flowing through each layer of the primary winding as those are connected in series. With a unit winding factor, the current flowing in the secondary winding is the same as the current in the primary winding but directed in the opposite direction. By *Ampere's law*, a magnetic flux is generated between each layer. This flux is proportional to the *magneto-motive force (MMF)*. It increases along the primary winding and decreases along the secondary winding (Figure A.9a). For the high frequency case (Figure A.9b), the same assumptions are made : diameter largely higher then *skin depth* ($d \gg \delta$) and the layers are very close. Thus, the same effect as previously is visible with an amplification along the layers. As before, eddy currents $i_{2,l} = -i_1 = i(t)$ are generated in the left side of the second wire w_2. However, as the net current in w_2 needs to be $i(t)$, the current in

the right side is $i_{2,r} = 2 \cdot i(t)$. Copper losses induced in w_2 is :

$$P_2 = I^2 R_{ac,2} + (2I)^2 R_{ac,2} = 5 \cdot P_1 \tag{A.30}$$

The same reasoning is done for the third wire w_3. But this time, the double amount of eddy currents are generated in w_3 because of $i_{2,r}$. This time, the losses generated in w_3 are :

$$P_3 = (2I)^2 R_{ac,2} + (3I)^2 R_{ac,2} = 13 \cdot P_1 \tag{A.31}$$

It is the same all over the layers in primary winding and then it decreases for secondary winding. The generalized copper loss formula for the m^{th} layer is :

$$P_m = I^2 \left[(m-1)^2 + m^2\right] \left(\frac{d}{4\delta} R_{dc}\right) \tag{A.32}$$

Total losses on a *M-layers* winding is then expressed as :

$$P = I^2 \left(\frac{d}{4\delta} R_{dc}\right) \sum_{m=1}^{M} \left[(m-1)^2 + m^2\right] \tag{A.33}$$

$$= I^2 \left(\frac{d}{4\delta} R_{dc}\right) \frac{M}{3}(2M^2 + 1) \tag{A.34}$$

Finally, the *proximity effect* increases losses by a factor :

$$F_R = \frac{P}{P_{dc}} = \frac{1}{3} \left(\frac{d}{4\delta}\right) (2M^2 + 1) \tag{A.35}$$

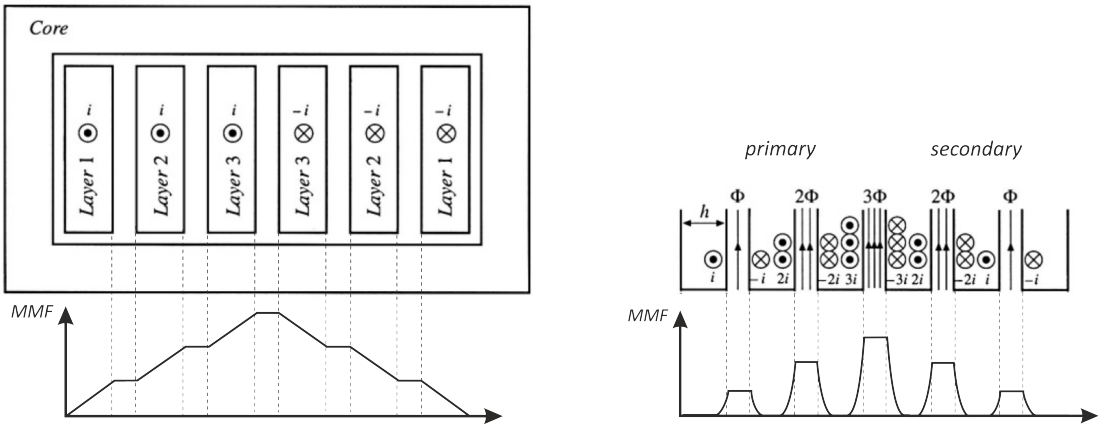

(a) Low-Frequency (net current i in each layer)[20] (b) High-frequency (net current i in each layer)[20]

Figure A.9 – Schematic representation of *Proximity effect* in a transformer

Case 2 : Dowell equation

When the diameter of a strand is not highly larger than the *skin depth*, the eddy-currents induced are not that large as previously. A straightforward formula is not possible to obtain for the *proximity factor (F_R)*. Then *Maxwell's equations* are used to evaluate an analytical equation of this factor also known as *Dowell equation* [27] :

$$F_R = \Delta \left[\frac{\sinh(2\Delta) + \sin(2\Delta)}{\cosh(2\Delta) - \cos(2\Delta)} + \frac{2}{3}(M^2 - 1)\frac{\sinh(\Delta) - \sin(\Delta)}{\cosh(\Delta) + \cos(\Delta)}\right] \tag{A.36}$$

with $\Delta = \sqrt{\frac{\pi}{4}}\frac{d}{\delta}$ the skin factor and $M = p * s$ the number of strand's layer s[1] contained in p winding layers (Figure A.10b).

[1]For a round wire composed of N_s strands, a good approximation is $s = \sqrt{N_s}$

Figure A.10a represents the evolution of *proximity factor* F_R with respect to the *skin factor* (Δ) and number of layers (M). An approximation of this equation for the case $\Delta < 1$ is given by [27] :

$$F_R = 1 + \frac{5M^2 - 1}{45}\Delta^4 \tag{A.37}$$

Those equations are analysed in section 2.3.

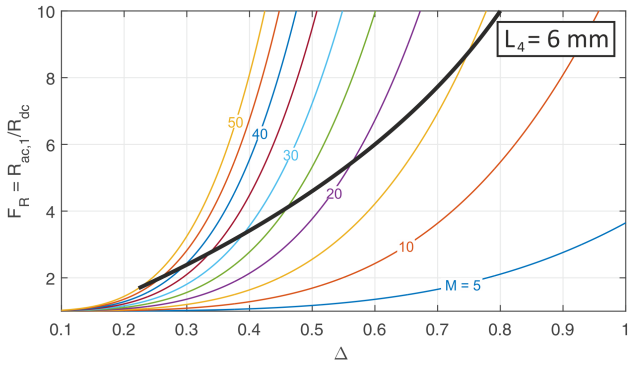

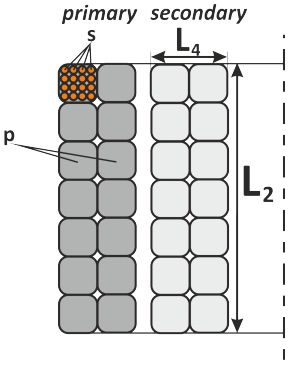

(a) *Proximity factor* (F_R) evolution with respect to *Skin factor* (Δ) and number of layers (M)

(b) Cross section representation of windings

Figure A.10

A.8 Thermal model : equivalent thermal conductivity of Litz Wire winding

The thermal resistance of windings is an important point for the thermal management. A high amount of heat is generated in those because of the electrical resistance. The problem is that the windings have a poor thermal conductivity because of insulation.

First, the heat generated by windings can flow in tangential direction which correspond to the winding direction. In that case, the heat flows to the winding endings. Even if the copper conductivity is high ($k_{cu} = 395$ $[W/mK]$), the windings are supposed to be long and with a relatively low cross section area, the tangential thermal resistance of the windings is too high.

So, the windings are cooled in both radial and axial directions only. However, the heat produced in each wire strand needs to flow through strand and wire insulation. Unfortunately, insulation which are used for their low electrical conductivity have also a low thermal conductivity ($k_{ins} = 0.15$ $[W/mK]$). Moreover, the wires in a winding for spatial application are impregnated with a resin in order to avoid the presence of vacuum space with zero conductivity inside the winding. The resins also have a low conductivity ($k_{res} = 0.15$ $[W/mK]$).

Figure A.11a represents the cross section of a winding with a zoom on a Litz wire. As it can be seen, each Litz strand is covered by an insulation (green) and each wire is also covered by an insulation (white). Between strands and wires the resin can be seen in yellow. The fill factors of winding and wire can be expressed as follows :

$$\begin{aligned} k_{f,wind} &= \frac{\text{wire area}}{\text{total winding area}} = N_w \cdot \frac{\pi \left(\frac{d_w}{2}\right)^2}{L_2 L_4} \\ k_{f,wire} &= \frac{\text{strand area}}{\text{total wire area}} = N_s \cdot \frac{d_s^2}{d_w^2} \end{aligned} \tag{A.38}$$

where N_w is the number of wire in the window, d_w is the wire diameter, N_s is the number of strands in a wire and d_s is the strand diameter.

In reality, wires and strands have a round cross section. However, it is too hard to compute the thermal resistances with round elements. In order to address the issue, the original winding is modelled with an equivalent simplified winding composed of the same number of wires, the same number of strands and, where each wire and strand is a square with same areas as the originals (Figure A.11b):

$$h_w = \sqrt{\frac{\pi}{4}} \cdot d_w \tag{A.39}$$

In that way, the heat flux is assumed to flows either in radial or axial directions. With square shapes, the thermal resistance of the composite winding is easier to compute.

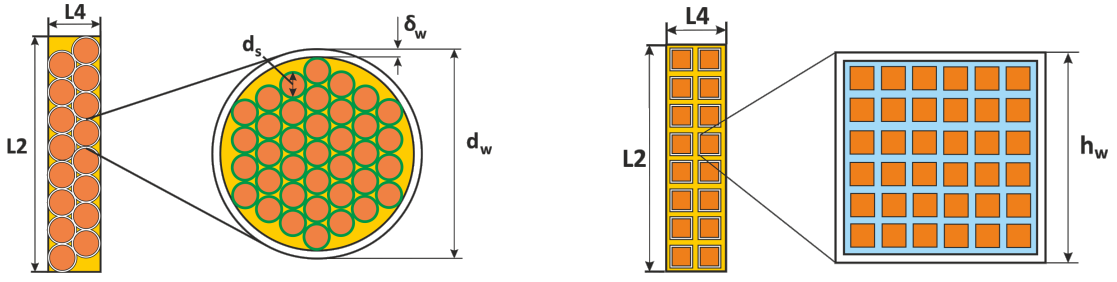

(a) Real winding (b) Equivalent winding

Figure A.11 – Cross section representation of the real and equivalent winding

First, an equivalent wire thermal conductivity needs to be obtained from the equivalent winding. It is logical than the same conductivity will be found for both radial and axial direction. Let's assume

that heat flows in axial direction (vertical direction in Figure A.11). The equivalent wire cross section can be divided into columns of two kind : columns composed of insulation and columns composed of alternation of strand and insulation. All columns can be represented by parallel thermal resistances. The composite columns themselves can be represented by series thermal resistances (alternation of strand and insulation). However, in a composite column the thermal resistance of strands can be neglected compared to the insulation thermal resistance as the thermal conductivity of copper is more than a thousand times higher than insulation thermal conductivity. An equivalent thermal resistance can be expressed as :

$$\begin{aligned} R_{th,wire,e} &= \sqrt{N_s} \cdot (R_{th,ins} // R_{th,comp}) \\ &= \frac{h_w \cdot (\sqrt{k_{f,wire}} + \sqrt{1-k_{f,wire}})}{k_{ins} \cdot L \cdot h_w \cdot \sqrt{1-k_{f,wire}}} // \frac{h_w \cdot \sqrt{1-k_{f,wire}}}{k_{ins} \cdot L \cdot h_w \cdot \sqrt{k_{f,wire}}} \\ &= \frac{\sqrt{1-k_{f,wire}}}{k_{ins} \cdot L \cdot \left(\frac{1-k_{f,wire}}{\sqrt{k_{f,wire}}+\sqrt{1-k_{f,wire}}} + \sqrt{k_{f,wire}} \right)} \end{aligned} \tag{A.40}$$

where L is the wire length. Considering (2.42), the equivalent homogeneous wire conductivity is :

$$\begin{aligned} k_{wire} &= k_{ins} \cdot k_e \\ &= k_{ins} \cdot \frac{\left(\frac{(1-k_{f,wire}}{\sqrt{1-k_{f,wire}}+\sqrt{k_{f,wire}}} \right) + \sqrt{k_{f,wire}}}{\sqrt{1-k_{f,wire}}} \end{aligned} \tag{A.41}$$

where k_e is the equivalent corrective factor of thermal conductivity. For a Litz wire with fill factor of $k_{f,wire} = 0.44$, the corrective factor is $k_e = 1.42$. This value really make sense because it means that the thermal resistance of wire is very close to the insulation. This is due to the low insulation conductivity which influence the result.

The same approach can be followed for the thermal resistance of the winding. The equivalent winding cross section can be divided into columns of two kind : columns with only insulation and columns with alternation of wire and insulation. All columns can be represented by parallel thermal resistances. The composite columns themselves can be represented by series thermal resistance (alternation of wire and insulation). This time, the wire does not have a conductivity highly better than insulation. So, it cannot be neglected. The equivalent thermal resistance of winding in axial direction can be expressed as :

$$\begin{aligned} R_{th,wind,a} &= N_{w,a} \cdot (R_{th,ins} // R_{th,comp}) \\ &= \frac{L_2 \cdot (\sqrt{k_{f,wind}} + \sqrt{1-k_{f,wind}})}{k_{ins} \cdot L \cdot L_4 \cdot \sqrt{1-k_{f,wind}}} // \frac{L_2 \cdot (\sqrt{1-k_{f,wire}} + k_e^{-1}\sqrt{k_{f,wind}}}{k_{ins} \cdot L \cdot L_4 \cdot \sqrt{k_{f,wire}}} \\ &= \frac{L_2}{k_{ins} \cdot L \cdot L_4} \cdot \left(1 + \frac{(k_e^{-1}-1) \cdot \sqrt{k_{f,wind}}}{1+(k_e^{-1}+1) \cdot \sqrt{1-k_{f,wind}}} \right) \end{aligned} \tag{A.42}$$

where $N_{w,a}$ is the number of wire in axial direction. Once again, an equivalent homogeneous winding conductivity is :

$$k_{wind} = k_{ins} \cdot \left(1 + \frac{(k_e^{-1}-1) \cdot \sqrt{k_{f,wind}}}{1+(k_e^{-1}+1) \cdot \sqrt{1-k_{f,wind}}} \right)^{-1} \tag{A.43}$$

For a winding made of Litz wire with fill factor $k_{f,wire} = 0.44$ and winding fill factor $k_{f,wind} = 0.75$, this winding conductivity is $k_{wind} = 1.17 \cdot k_{ins}$. So, in a classic winding, the thermal resistance is about 15% better than the case of a winding filled of insulation only. This thermal conductivity can be applied for winding thermal resistance in radial direction with (2.43) :

$$R_{th,wind,r} = \frac{\ln\left(\frac{r_i+L_4}{r_i}\right)}{k_{ins} \cdot 2\pi L_2} \cdot \left(1 + \frac{(k_e^{-1}-1) \cdot \sqrt{k_{f,wind}}}{1+(k_e^{-1}+1) \cdot \sqrt{1-k_{f,wind}}} \right) \tag{A.44}$$

where r_i is the inner radius of winding.

A.9 Thermal model : thermal resistances calculations

This appendix is dedicated to the expression derivation for the equivalent components of the transformer thermal model. First, the distance expression between each geometry part node and the axis is presented in table A.1. Then, the thermal resistances involved in the node network are expressed in table A.2.

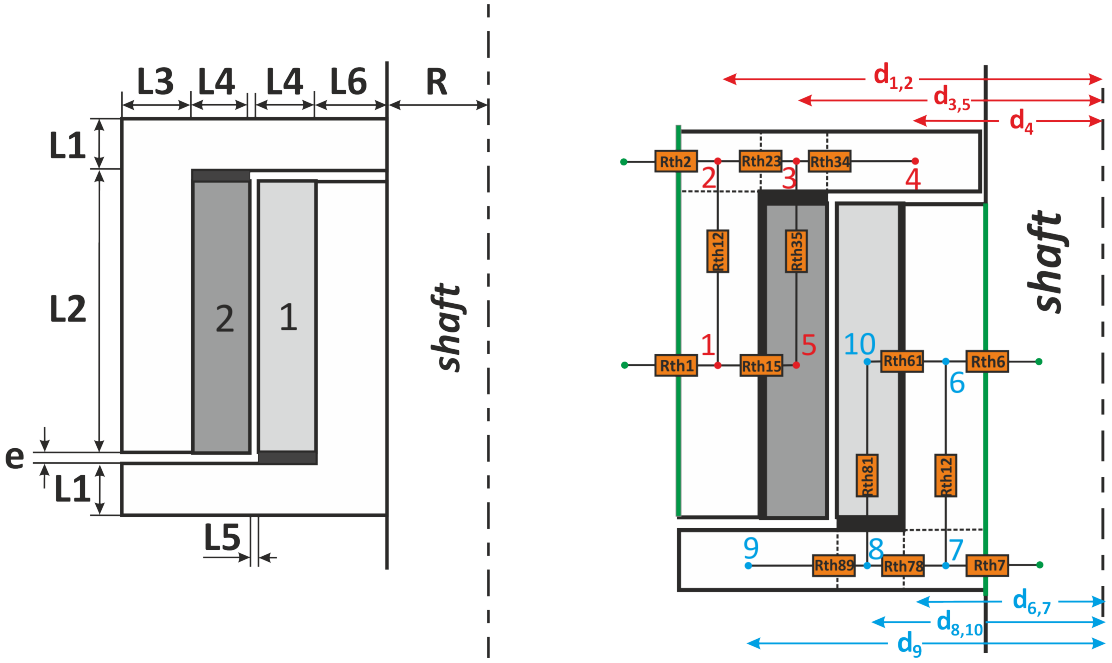

(a) Transformer dimensions

(b) Thermal circuit representation

Figure A.12 – Thermal resistance calculation : thermal circuit representation

Distance to the axis	Expression
d_1	$\sqrt{\frac{(R+2*L_4+L_5+L_6)^2+(R+L_3+2*L_4+L_5+L_6)^2}{2}}$
d_2	$\sqrt{\frac{(R+2*L_4+L_5+L_6)^2+(R+L_3+2*L_4+L_5+L_6)^2}{2}}$
d_3	$\sqrt{\frac{(R+L_4+L_5+L_6)^2+(R+2*L_4+L_5+L_6)^2}{2}}$
d_4	$\sqrt{\frac{R^2+(R+L_4+L_5+L_6)^2}{2}}$
d_5	$\sqrt{\frac{(R+L_4+L_5+L_6)^2+(R+2*L_4+L_5+L_6)^2}{2}}$
d_6	$\sqrt{\frac{R^2+(R+L_6)^2}{2}}$
d_7	$\sqrt{\frac{R^2+(R+L_6)^2}{2}}$
d_8	$\sqrt{\frac{(R+L_6)^2+(R++L_4)^2}{2}}$
d_9	$\sqrt{\frac{(R+L_4+L_6)^2+(R+L_3+2*L_4+L_5+L_6)^2}{2}}$
d_{10}	$\sqrt{\frac{(R+L_6)^2+(R++L_4)^2}{2}}$

Table A.1 – Reluctance model : distance between nodes and the axis

Distance to the axis	**Expression**
$R_{th,1}$	$\frac{ln\left(\frac{R+L_3+2*L_4+L_5+L_6}{d_1}\right)}{2\pi L_2 \cdot k_{fer}}$
$R_{th,12}$	$\frac{\left(\frac{L_1+L_2}{2}\right)}{L_3 \cdot d_1 \cdot k_{fer}}$
$R_{th,15}$	$\frac{ln\left(\frac{d_1}{R+2*L_4+L_5+L_6}\right)}{2\pi L_2 \cdot k_{fer}} + \frac{ln\left(\frac{R+2*L_4+L_5+L_6}{d_5}\right)}{2\pi L_2 \cdot k_{wind}} + \frac{\delta_{glue}}{2\pi(R+2*L_4+L_5+L_6) \cdot L_2 \cdot k_{glue}}$
$R_{th,2}$	$\frac{ln\left(\frac{R+L_3+2*L_4+L_5+L_6}{d_2}\right)}{2\pi L_1 \cdot k_{fer}}$
$R_{th,23}$	$\frac{ln\left(\frac{d_2}{d_3}\right)}{2\pi L_1 \cdot k_{fer}}$
$R_{th,34}$	$\frac{ln\left(\frac{d_3}{d_4}\right)}{2\pi L_1 \cdot k_{fer}}$
$R_{th,35}$	$\frac{\frac{L_2}{2*k_{wind}}+\frac{L_1}{2*k_{fer}}+\frac{\delta_{glue}}{k_{glue}}}{2\pi d_3 \cdot L_4}$
$R_{th,6}$	$\frac{ln\left(\frac{R}{d_6}\right)}{2\pi L_2 \cdot k_{fer}}$
$R_{th,67}$	$\frac{\left(\frac{L_1+L_2}{2}\right)}{L_6 \cdot d_6 \cdot k_{fer}}$
$R_{th,61}$	$\frac{ln\left(\frac{d_6}{R+L_6}\right)}{2\pi L_2 \cdot k_{fer}} + \frac{ln\left(\frac{R+L_6}{d_5}\right)}{2\pi L_2 \cdot k_{wind}} + \frac{\delta_{glue}}{2\pi(R+L_6) \cdot L_2 \cdot k_{glue}}$
$R_{th,7}$	$\frac{ln\left(\frac{R}{d_7}\right)}{2\pi L_1 \cdot k_{fer}}$
$R_{th,78}$	$\frac{ln\left(\frac{d_8}{d_7}\right)}{2\pi L_1 \cdot k_{fer}}$
$R_{th,89}$	$\frac{ln\left(\frac{d_9}{d_8}\right)}{2\pi L_1 \cdot k_{fer}}$
$R_{th,81}$	$\frac{\frac{L_2}{2*k_{wind}}+\frac{L_1}{2*k_{fer}}+\frac{\delta_{glue}}{k_{glue}}}{2\pi d_8 \cdot L_4}$

Table A.2 – Reluctance model : reluctances expression

B.1 Solar Array Drive Mechanism : RUAG Septa 24®

SEPTA® 24
Solar Array Drive Assembly

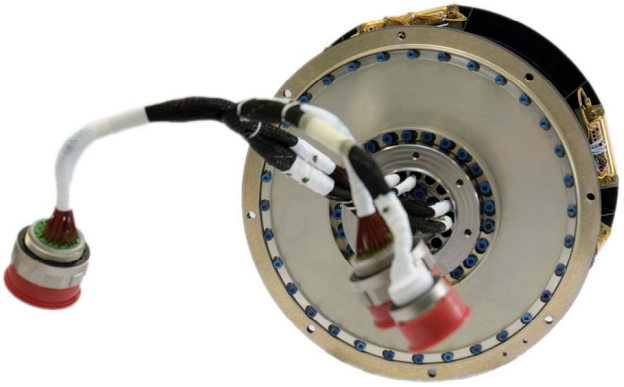

RUAG Space | Schaffhauserstrasse 580 | CH-8052 Zurich | Switzerland
Phone +41 44 306 2211 | info.space@ruag.com | www.ruag.com/space

Together ahead. RUAG

DESIGN CHARACTERISTICS

Operational performance	
Drive direction	Forward and reverse full rotation
Output speed range (nominal in orbit)	0 to 20 revs per day
Maximum output speed (ground testing)	0.75 °/s
Stabile positions at input shaft (with motor unpowered)	360 steps over a full revolution
1 output step between to stabile positions	0.00625°
1 full rotation range (at output shaft)	57600 output steps
Life span	15 years in orbit + 5 year storage (2 years integrated on S/C)
Revolutions performance	250 on ground 5475 orbital full revs (1 revs / day)
Qualification sequence	1000 + 11000 = 12000 full revs

Delivered torque	
SA holding torque with motor unpowered	up to 7 Nm
SA holding torque with motor powered	≥ 70 Nm
SA driving torque (motor powered)	up to 35 Nm
Limit for repeated peak torque	64 Nm (starting and stop)
Limit for momentary peak torque	76 Nm (exceptional peak torque)

Power Transfer	
Number of power transfers (forward & return lines)	12 or 24 transfers
Current	7.5 A or 10 A
Voltage	up to 110 V (250 V resistant)
Power transfer	up to 19.8 kW
Total line resistance at 20 °C (incl. external harness)	29 mΩ (max.)
Total line resistance in the worst hot case (incl. external harness)	38 mΩ (max.)
Insulation	≥ 10 MΩ at 500 V
Noise	≤ 5 mV_{RMS}/A

Signal Transfer	
Number of signal transfers (forward & return lines)	34
SA Ground lines	2
Current	0.5 A for signals (1.0 A with MIL derating) 1.0 A for SA ground
Voltage	55 V
Total line resistance at 20 °C (incl. external harness)	90 mΩ
Total line resistance in the worst hot case (incl. external harness)	105 mΩ
Insulation	≥ 10 MΩ at 500 V
Noise	≤10 mV_{RMS}/A

B.2 Power Conditioning Unit Next Generation

ThalesAlenia Space
A Thales / Finmeccanica Company

Power Conditioning Unit Next Generation

Applications

- The Power Conditioning Unit (PCU) is used for medium to very high power geostationary satellites (6 to 21KW), like the Thales Alenia Space Spacebus 4000 family. This product is under development to improve the PCU 4000 competitiveness and performances.

Main features

- Generation of a precisely and fully regulated bus during sunlight and eclipse.
- Three domains control concept ensuring :
  - Smooth transition between battery charge, sunlight and eclipse modes of operation
  - Control of the battery charge current according to solar array power margin
- Mechanical modularity to adapt to solar array and bus power need.
- High efficiency for solar array, batteries and thermal management optimization.
- High reliability thanks to tolerance to any part failure.
- Battery isolation for satellite power off during integration.

Production

- Capacity : 6 per year
- Typical schedule : 12 months

Technical description

- Upmost recent qualified technologies and designs
- **Sunlight periods** :
  - Control of the power delivered by the solar array generators (9 to 24 sections) through a series redunded Sequential Switching Shunt Regulators (S3R). No failure leads to lose any SA power on the bus.
  - Recharge of the batteries via modular current controlled Battery Charge Regulators (BCR).
- **Eclipses periods** :
  - The power is delivered by one or two lithium Ion batteries and the bus regulation is performed by 4 to 14 Battery Discharge Regulators (3 to 7 BDR's per battery)

Background

- Development on-going.
- Qualification in 2013 and first flight models in 2014

THALES

PCU NG TYPICAL PERFORMANCES

PARAMETER	PERFORMANCES
PCU power output	5,4 -21,6 kW, by step of 1.8 kW
Bus voltage	100V +1V/-0V (PCU) (fully regulated, 3 domains control)
Bus impedance (typical)	< 25 mΩ
Bus voltage ripple	< 500 mVpp
Sun regulation (S3R)	6 A < solar array section current < 16 A 9 < number of solar array sections < 24 Solar array parasitic capacitance < 0,2 uF/A Series redunded (no loss of SA power after failure)
Battery types	Li Ion
Battery voltage	54 V < V battery < 98.5 V
Battery charge current	7.5A < battery charge current < 35A max. (17.5A per battery)
Battery management	By on-board computer or autonomous voltage tapering at PCU level
PCU Efficiency	Solar Array > 99 % Battery discharge > 96 % Battery charge > 96 %
PCU mass for 21,6 kW output power	< 51 kg

AUTOMATISMS AND PROTECTIONS

Battery end of charge automatism (overridable)	Battery Li Ion : over-voltage criterion and automatic EoC tapering (option)
Battery charge & discharge regulators	Internal resettable protections
Bus overvoltage protection	Connection of a resistive load on the bus (resettable).

This datasheet is not contractual and can be changed without any notice *Updated May 2012*

For further information, please contact

Thales Alenia Space ETCA
101, rue Chapelle Beaussart
B-6032 Mont-sur-Marchienne - Belgium
Tel.: + 32(0)71 44 23 11
Fax: + 32(0)71 44 22 00
E-mail : etca.info@thalesaleniaspace.com
Website : www.thalesaleniaspace.com

B.3 Dual Active Bridge Transistor : SiC MOSFET

CREE

CPM2-1200-0025B

Silicon Carbide Power MOSFET
C2M™ MOSFET Technology
N-Channel Enhancement Mode

V_{DS}	1200 V
$I_{D\ @\ 25°C}$	98 A
$R_{DS(on)}$	25 mΩ

Features

- High Blocking Voltage with Low On-Resistance
- High Speed Switching with Low Capacitances
- Easy to Parallel and Simple to Drive
- Avalanche Ruggedness
- Resistant to Latch-Up
- Halogen Free, RoHS Compliant

Benefits

- Higher System Efficiency
- Reduced Cooling Requirements
- Increased Power Density
- Increased System Switching Frequencyy

Applications

- Solar Inverters
- Switch Mode Power Supplies
- High Voltage DC/DC converters
- Battery Chargers
- Motor Drive
- Pulsed Power Applications

Chip Outline

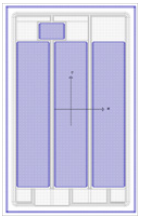

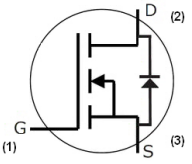

Part Number	Die Size (mm)
CPM2-1200-0025B	4.04 x 6.44

Maximum Ratings (T_C = 25 ˚C unless otherwise specified)

Symbol	Parameter	Value	Unit	Test Conditions	Note
V_{DSmax}	Drain - Source Voltage	1200	V	V_{GS} = 0 V, I_D = 100 µA	
V_{GSmax}	Gate - Source Voltage	-10/+25	V	Absolute maximum values, AC (f >1 Hz)	
V_{GSop}	Gate - Source Voltage	-5/+20	V	Recommended operational values	
I_D	Continuous Drain Current	98	A	V_{GS} =20 V, T_C = 25˚C	Note 1
		71		V_{GS} =20 V, T_C = 100˚C	
$I_{D(pulse)}$	Pulsed Drain Current	250	A	Pulse width t_P limited by T_{jmax}	
T_J , T_{stg}	Operating Junction and Storage Temperature	-40 to +175	˚C		
T_{Proc}	Maximum Processing Temperature	325	˚C	10 min. maximum	

Note (1): Assumes a $R_{\theta JC}$ < 0.27 K/W

CREE

Electrical Characteristics (T_C = 25˚C unless otherwise specified)

Symbol	Parameter	Min.	Typ.	Max.	Unit	Test Conditions	Note
$V_{(BR)DSS}$	Drain-Source Breakdown Voltage	1200			V	V_{GS} = 0 V, I_D = 100 µA	
$V_{GS(th)}$	Gate Threshold Voltage	2.0	2.6	4	V	V_{DS} = V_{GS}, I_D = 15mA	Fig. 11
			2.0		V	V_{DS} = V_{GS}, I_D = 15mA, T_J = 175 °C	
I_{DSS}	Zero Gate Voltage Drain Current		2	100	µA	V_{DS} = 1200 V, V_{GS} = 0 V	
I_{GSS}	Gate-Source Leakage Current			600	nA	V_{GS} = 20 V, V_{DS} = 0 V	
$R_{DS(on)}$	Drain-Source On-State Resistance		25	34	mΩ	V_{GS} = 20 V, I_D = 50 A	Fig. 4,5,6
			52			V_{GS} = 20 V, I_D = 50 A, T_J = 175 °C	
g_{fs}	Transconductance		23.6		S	V_{DS}= 20 V, I_{DS}= 50 A	Fig. 7
			21.1			V_{DS}= 20 V, I_{DS}= 50 A, T_J = 175 °C	
C_{iss}	Input Capacitance		2788		pF	V_{GS} = 0 V V_{DS} = 1000 V f = 1 MHz V_{AC} = 25 mV	Fig. 17,18
C_{oss}	Output Capacitance		220				
C_{rss}	Reverse Transfer Capacitance		15				
E_{oss}	C_{oss} Stored Energy		121		µJ		Fig 16
E_{AS}	Avalanche Energy, Single Pluse		3.5		J	I_D = 50A, V_{DD} = 50V	
E_{ON}	Turn-On Switching Energy		1.4		mJ	V_{DS} = 800 V, V_{GS} = -5/20 V, I_D = 50A, $R_{G(ext)}$ = 2.5Ω,L= 412 µH	
E_{OFF}	Turn Off Switching Energy		0.3				
$t_{d(on)}$	Turn-On Delay Time		14		ns	V_{DD} = 800 V, V_{GS} = -5/20 V I_D = 50 A, $R_{G(ext)}$ = 2.5 Ω, R_L = 16 Ω Timing relative to V_{DS} Per IEC60747-8-4 pg 83	
t_r	Rise Time		32				
$t_{d(off)}$	Turn-Off Delay Time		29				
t_f	Fall Time		28				
$R_{G(int)}$	Internal Gate Resistance		1.1		Ω	f = 1 MHz, V_{AC} = 25 mV, ESR of C_{ISS}	
Q_{gs}	Gate to Source Charge		46		nC	V_{DS} = 800 V, V_{GS} = -5/20 V I_D = 50 A Per IEC60747-8-4 pg 83	Fig. 12
Q_{gd}	Gate to Drain Charge		50				
Q_g	Total Gate Charge		161				

Reverse Diode Characteristics

Symbol	Parameter	Typ.	Max.	Unit	Test Conditions	Note
V_{SD}	Diode Forward Voltage	4.0		V	V_{GS} = - 5 V, I_{SD} = 25 A	Fig. 8, 9, 10
		3.5		V	V_{GS} = - 5 V, I_{SD} = 25 A, T_J = 175 °C	
I_S	Continuous Diode Forward Current		98		T_C= 25 °C	Note 2
t_{rr}	Reverse Recovery Time	45		ns	V_{GS} = - 5 V, I_{SD} = 50 A ,T_J = 25 °C VR = 800 V dif/dt = 1000 A/µs	Note 2
Q_{rr}	Reverse Recovery Charge	406		nC		
I_{rrm}	Peak Reverse Recovery Current	13.5		A		

Note (2): When using SiC Body Diode the maximum recommended V_{GS} = -5V

Note (3): For inductive and resistive switching data and waveforms please refer to datasheet for packaged device. Part number C2M0025120D.

B.4 Rupalit Litz Wire

Structure		External diameter without wrapping		External diameter with wrapping 1 x 52 (1 x Natural silk)		2 x 52 (2 x Natural silk)		Cross-section	DC-Resistance at 20°C (68°F)			Metres per kg
No. of strands	diameter of single wire [mm]	min [mm]	max [mm]	min [mm]	max [mm]	min [mm]	max [mm]	[mm²]	min [Ω/km]	nmo [Ω/km]	max [Ω/km]	nom [m/kg]
	0.016 AWG 54	Other dimensions on request										
	0.020 AWG 52	Other dimensions on request										
	0.022 AWG 51	Other dimensions on request										
	0.025 AWG 50	Other dimensions on request										
10		0.127	0.142	0.157	0.177	0.187	0.212	0.00707	2176	2467	2713	11764
20		0.179	0.200	0.209	0.235	0.239	0.270	0.01414	1088	1233	1357	6060
25								0.01767				4964
30								0.02121				3921
35				External diameter depending on type				0.02474				3355
45				of wrapping. Dimensions on request				0.03181				2611
60	0.03							0.04241				1960
75								0.05301				1567
90	AWG 48							0.06362				1307
105								0.07422				1119
120								0.08482				980
135								0.09542				871
180								0.12723				653
225								0.15904				522
270								0.19085				435
Other types of litz wire up to external diameter 11 mm on request												
10		0.164	0.186	0.194	0.221	0.224	0.256	0.01282	1228	1387	1522	7847
12		0.183	0.208	0.213	0.243	0.243	0.278	0.1538	1023	1156	1268	6536
15		0.201	0.229	0.236	0.269	0.261	0.299	0.01923	819	925	1015	5229
20		0.232	0.264	0.267	0.304	0.292	0.334	0.02564	614	694	761	3922
25		0.260	0.295	0.295	0.335	0.320	0.365	0.03204	491	555	609	3137
30		0.284	0.323	0.319	0.363	0.344	0.393	0.03845	409	462	522	2615
35		0.307	0.349	0.342	0.389	0.367	0.419	0.04486	351	396	448	2241
45	0.04	0.348	0.395	0.383	0.435	0.408	0.465	0.0768	273	308	348	1743
60		0.405	0.460	0.440	0.500	0.465	0.530	0.07691	205	231	266	1231
75	AWG 46	0.453	0.515	0.488	0.555	0.513	0.585	0.09613	164	185	213	985
90		0.497	0.565	0.532	0.605	0.567	0.645	0.11536	136	154	178	821
105		0.537	0.610	0.572	0.650	0.607	0.690	0.13459	117	132	152	704
120		0.572	0.650	0.607	0.690	0.642	0.730	0.15381	102	116	133	615
135		0.607	0.690	0.642	0.730	0.677	0.770	0.17304	91	103	118	547
180		0.722	0.820	0.757	0.860	0.792	0.900	0.23072	68	77	90	385
225		0.805	0.915	0.840	0.955	0.895	1.015	0.28840	55	62	72	308
270		0.884	1.005	0.919	1.045	0.974	1.105	0.34608	45.5	51.4	60.3	257
Other types of litz wire up to external diameter 11 mm on request												
6		0.162	0.179	0.192	0.214	0.222	0.249	0.01202	1320	1480	1613	8505
8		0.186	0.206	0.216	0.241	0.246	0.276	0.01602	990	1100	1210	6379
10		0.209	0.231	0.244	0.271	0.269	0.301	0.02003	792	888	968	5103
12		0.232	0.257	0.267	0.297	0.292	0.327	0.02403	660	740	807	4253
15		0.256	0.283	0.291	0.323	0.316	0.353	0.03004	528	592	645	3402
20		0.295	0.327	0.330	0.367	0.355	0.397	0.04006	396	444	484	2552
25		0.330	0.366	0.365	0.406	0.390	0.436	0.05007	317	355	387	2041
30		0.382	0.401	0.397	0.441	0.422	0.471	0.06008	264	296	332	1701
35	0.05	0.391	0.433	0.426	0.473	0.451	0.503	0.07010	226	254	285	1458
45		0.443	0.490	0.478	0.530	0.503	0.560	0.09012	176	197	222	1134
60	AWG 44	0.515	0.570	0.550	0.610	0.585	0.650	0.12017	132	148	169	801
75		0.577	0.639	0.612	0.679	0.647	0.719	0.15021	106	118	136	641
90		0.633	0.701	0.668	0.741	0.703	0.781	0.18025	88	99	113	534
105		0.683	0.756	0.718	0.796	0.753	0.836	0.21029	75	85	97	458
120		0.728	0.806	0.763	0.846	0.798	0.886	0.24033	66	74	85	400
135		0.773	0.856	0.808	0.896	0.863	0.956	0.27037	59	66	75	356
180		0.918	1.017	0.953	1.057	1.008	1.117	0.36050	44.0	49.3	57.6	250
225		1.025	1.135	1.060	1.175	1.115	1.235	0.45062	35.2	39.5	46.0	200
270		1.126	1.246	1.161	1.286	1.216	1.346	0.54075	29.3	32.9	38.4	167
Other types of litz wire up to external diameter 11 mm on request												
3		0.163	0.189	0.193	0.224	0.223	0.259	0.01212	1331	1468	1578	8537
5		0.205	0.238	0.240	0.278	0.265	0.308	0.02019	799	881	947	5122
6		0.220	0.254	0.255	0.294	0.280	0.324	0.02423	666	734	789	4268
8		0.253	0.293	0.288	0.333	0.313	0.363	0.03231	499	551	592	3201
10		0.283	0.328	0.318	0.368	0.343	0.88	0.4038	399	440	473	2561
12		0.315	0.365	0.350	0.405	0.375	0.435	0.04846	333	367	394	2134
15		0.347	0.402	0.382	0.442	0.407	0.472	0.06058	266	294	316	1702
20		0.401	0.464	0.436	0.504	0.461	0.534	0.08077	200	220	237	1280
25		0.448	0.519	0.483	0.559	0.508	0.589	0.10096	160	176	189	1024
30		0.491	0.568	0.526	0.608	0.561	0.648	0.12115	133	147	163	854
35		0.530	0.614	0.565	0.654	0.600	0.694	0.14134	114	126	139	732
45		0.601	0.696	0.636	0.736	0.671	0.776	0.18173	89	98	108	570
60		0.699	0.810	0.734	0.850	0.769	0.890	0.24230	67	73	83	402
75		0.783	0.906	0.813	0.946	0.873	1.006	0.30288	53	59	66	322
90		0.859	0.994	0.894	1.034	0.949	1.094	0.36345	44.4	48.9	55.2	268
105		0.927	1.074	0.962	1.114	1.017	1.174	0.42403	38.0	41.9	47.3	230
120	0.071	0.988	1.144	1.023	1.184	1.078	1.244	0.48461	33.3	36.7	41.4	201
135		1.049	1.214	1.084	1.254	1.139	1.314	0.54518	29.6	32.6	36.8	179
180	AWG 41	1.246	1.443	1.281	1.483	1.336	1.543	0.72691	22.2	24.5	28.2	126
225		1.391	1.610	1.426	1.650	1.481	1.710	0.90864	17.8	19.6	22.5	107
270		1.528	1.769	1.563	1.809	1.618	1.869	1.09036	14.8	16.3	18.8	94
315		1.649	1.910	1.684	1.950	1.739	2.010	1.27209	12.7	14.0	16.1	72
405		1.870	2.165	1.905	2.205	1.960	2.265	1.63555	9.9	10.9	12.5	56
420			2.13					1.67	9.5	10.5	11.3	54
525			2.39	External diameter depending on type				2.08	7.6	8.4	9.0	43
630			2.61	of wrapping. Dimensions on request				250	6.3	7.0	7.5	36
735			2.82					2.92	5.4	6.0	6.4	31
840			3.03					3.33	4.8	5.2	5.6	27
945			3.20					3.75	4.3	4.7	5.0	24
1260			3.70					5.00	3.2	3.5	3.8	17
1575			4.15					6.21	2.5	2.8	3.0	13
1890			4.55					7.49	2.1	2.3	2.5	11
2205			4.86					8.74	1.8	2.0	2.1	10
2835			5.60					11.23	1.4	1.6	1.7	7.5

PACK Feindrähte

Rudolf Pack GmbH & Co.
Am Bäuweg 9-11
D-51645 Gummersbach

Tel.: +49/(0) 22 61/95 67- 0
Fax: +49/(0) 22 61/95 67-67

www.pack-feindraehte.de
info@pack-feindraehte.de

Technical Data

RUPALIT® Litz wire

(The technical data comply in part with the specification given in standard IEC 60317-11)

RUPALIT® high-frequency litz wires are constructed from enamelled copper wire (magnet wire) made of RUPOL®, RUPEX® or RUTHERM® – see illustrations below. (Aluminium magnet wires on request)

On special request, we can also supply any other design of litz wire up to an overall cross-section of 1.000 mm²

For further information, please refer to our Data Sheets

RUPALIT®

RUPALIT®

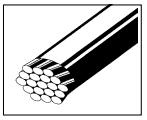

RUPALIT® Profile

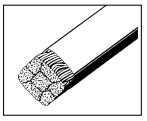

RUPALIT® Planar

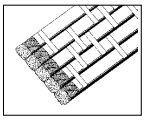

RUPALIT® Safety (IEC 60950)

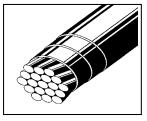

RUPALIT® Safety Profile (IEC 60950)

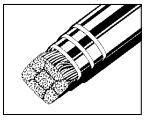

RUPALIT® Braided

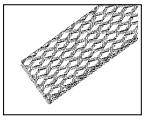

RUPALIT® 05

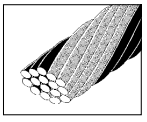

RUPOL® Safety (IEC 60950)

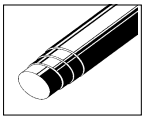

RUPA® Profile

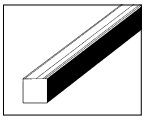

B.5 Ferroxcube 3C90 Ferrite : Material Specifications

3C90 SPECIFICATIONS

A low frequency power material for use in power and general purpose transformers at frequencies up to 0.2 MHz.

	CONDITIONS	VALUE	UNIT
μ_i	25 °C; ≤10 kHz; 0.25 mT	2300 ±20%	
μ_a	100 °C; 25 kHz; 200 mT	5500 ±25%	
B	25 °C; 10 kHz; 1200 A/m	≈ 470	mT
	100 °C; 10 kHz; 1200 A/m	≈ 380	mT
P_V	100 °C; 25 kHz; 200 mT	≤ 80	kW/m^3
	100 °C; 100 kHz; 100 mT	≤ 80	
	100 °C; 100 kHz; 200 mT	≈ 450	
ρ	DC, 25 °C	≈ 5	Ωm
T_C		≥ 220	°C
density		≈ 4800	kg/m^3

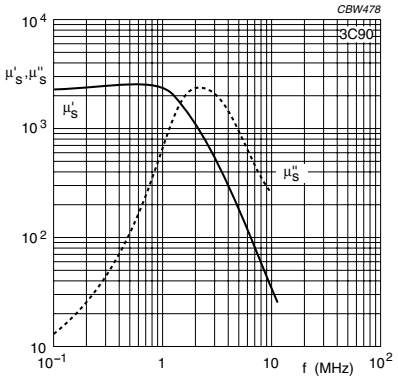

Fig.1 Complex permeability as a function of frequency.

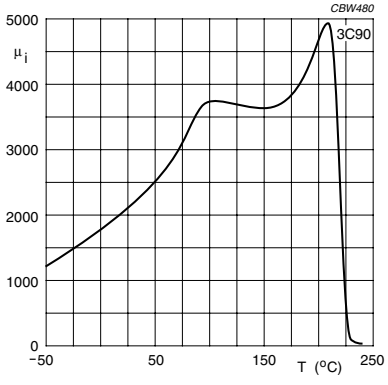

Fig.2 Initial permeability as a function of temperature.

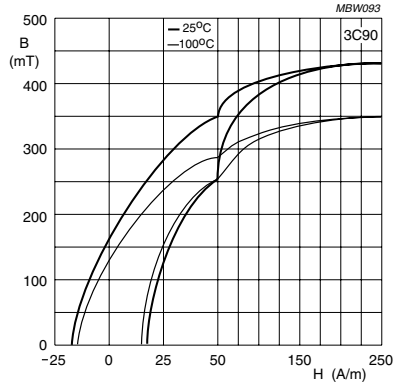

Fig.3 Typical B-H loops.

B.6 Ferroxcube 3C92 Ferrite : Material Specifications

3C92 SPECIFICATIONS

A low frequency, high Bsat power material for use in power inductors at frequencies up to 0.2 MHz.

SYMBOL	CONDITIONS	VALUE	UNIT
μ_i	25 °C; ≤10 kHz; 0.25 mT	1500 ±20%	
μ_a	100 °C; 25 kHz; 200 mT	≈ 5000	
B	25 °C; 10 kHz; 1200 A/m	≈ 540	mT
	100 °C; 10 kHz; 1200 A/m	≈ 460	
	140 °C; 10 kHz; 1200 A/m	≈ 400	
P_V	100 °C; 100 kHz; 100 mT	≈ 50	kW/m^3
	100 °C; 100 kHz; 200 mT	≈ 350	
ρ	DC; 25 °C	≈ 5	Ωm
T_C		≥ 280	°C
density		≈ 4800	kg/m^3

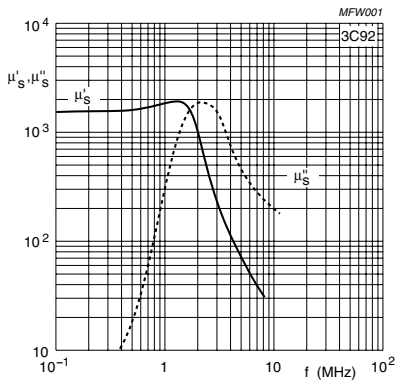

Fig.1 Complex permeability as a function of frequency.

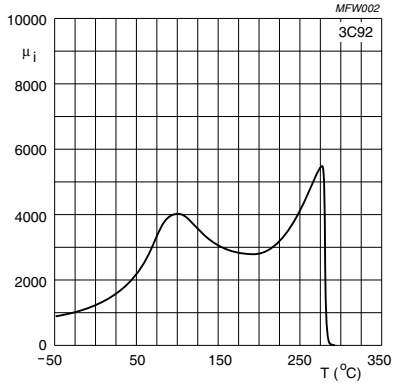

Fig.2 Initial permeability as a function of temperature.

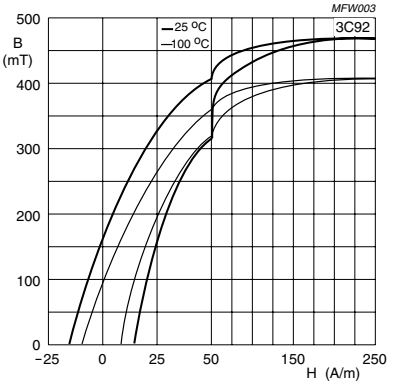

Fig.3 Typical B-H loops.

B.7 Ferroxcube Ferrite : E71/33/32

CORE SETS

Effective core parameters

SYMBOL	PARAMETER	VALUE	UNIT
Σ(l/A)	core factor (C1)	0.218	mm^{-1}
V_e	effective volume	102000	mm^3
l_e	effective length	149	mm
A_e	effective area	683	mm^2
A_{min}	minimum area	676	mm^2
m	mass of core half	≈ 260	g

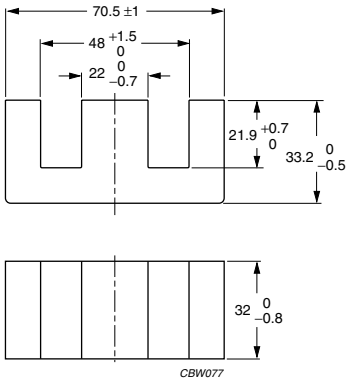

Dimensions in mm.

Fig.1 E71/33/32 core half.

Core halves

A_L measured in combination with a non-gapped core half, clamping force for A_L measurements 60 ±20 N, unless stated otherwise.

GRADE	A_L (nH)	μ_e	TOTAL AIR GAP (μm)	TYPE NUMBER
3C90	100 ±5%(1)	≈ 17	≈ 17800	E71/33/32-3C90-E100
	160 ±5%(1)	≈ 28	≈ 9620	E71/33/32-3C90-E160
	250 ±5%(1)	≈ 43	≈ 5280	E71/33/32-3C90-E250
	315 ±5%(1)	≈ 55	≈ 3900	E71/33/32-3C90-E315
	400 ±8%(1)	≈ 69	≈ 2860	E71/33/32-3C90-E400
	630 ±10%(1)	≈ 109	≈ 1620	E71/33/32-3C90-E630
	10800 ±25%	≈ 1880	≈ 0	E71/33/32-3C90
3C92 des	8000 ±25%	≈ 1390	≈ 0	E71/33/32-3C92
3C94	10800 ±25%	≈ 1880	≈ 0	E71/33/32-3C94
3C95 des	13330 ±25%	≈ 2315	≈ 0	E71/33/32-3C95
3F3	100 ±5%(1)	≈ 17	≈ 17800	E71/33/32-3F3-E100
	160 ±5%(1)	≈ 28	≈ 9620	E71/33/32-3F3-E160
	250 ±5%(1)	≈ 43	≈ 5280	E71/33/32-3F3-E250
	315 ±5%(1)	≈ 55	≈ 3900	E71/33/32-3F3-E315
	400 ±8%(1)	≈ 69	≈ 2860	E71/33/32-3F3-E400
	630 ±10%(1)	≈ 109	≈ 1620	E71/33/32-3F3-E630
	10000 ±25%	≈ 1740	≈ 0	E71/33/32-3F3

Note

1. Measured in combination with an equal gapped core half.

Rue Archimède, 1 bte L6.11.01, 1348 Louvain-la-Neuve **www.uclouvain.be/epl**